**Article:**
Bacchetti, A., Lloyd, P., Brockdorff, M. et al. (2026) Tapered Magnetic Soft Continuum Catheters with Integrated Microchannels for Cerebral Intra-Arterial Chemotherapy Delivery. Soft Robotics. ISSN: 2169-5172

https://doi.org/10.1177/21695172261438681

# Tapered Magnetic Soft Continuum Catheters with Integrated Microchannels for Cerebral Intra-Arterial Chemotherapy Delivery

**Alistair Bacchetti, Peter Lloyd, Michael Brockdorff, Benjamin Calmé, Joshua Davy, Vittorio Francescon, Nikita Murasovs, Yael L. May, Ryan K. Mathew, Russell A. Harris, Pietro Valdastri and James H. Chandler**

**REVISED PROOFS (SUBMITTED 17TH MARCH 2026)**

**All bold/blue sections are previous approved changes from revision 1 (submitted 31st Oct 2025)**

## Abstract

Magnetic soft continuum robots offer the possibility for wireless manipulation, compliant shape-forming and miniaturization to the milli- and submillimeter scales. This presents them as an attractive choice in the development of robotic guidewires and catheters for endovascular applications. However, few approaches have considered strategies for geometric modification to enhance navigation and therapeutic delivery. These aspects are of high relevance for applications such as intra-arterial chemotherapeutic delivery. Here we present an octopus tentacle-inspired magnetic soft continuum robot with a monolithic material composition, tapered geometry of ≤2 mm, and integrated microchannels. We consider suitability of a discrete elastic modelling approach alongside Finite Element based and Material Point Method simulations for capturing the deflection behavior of the tapered design under magnetic actuation. The Material Point Method demonstrates the greatest accuracy, with root mean square errors in tip angle between 2.74° - 5.28°. For higher taper designs, experimental results highlight improved deflection under low magnetic field strengths (<5 mT) and an improved workspace at high actuation angles (up to 320°). We subsequently utilize tapered designs with a 0.66 mm distal tip diameter and embedded axial and lateral microchannel networks for localized drug simulant delivery in a neurovascular tumor phantom. We demonstrate significant improvements in localized drug delivery along specific vascular pathways in comparison to systemic intra-arterial delivery.

**Keywords:** Tapered: Soft Interaction, Soft Manipulation, Continuum Robot, Medical Robot, Highly Deformable Robots, Biomimetic Robots.

**Manuscript Keywords**: Tapered Magnetic Soft Continuum Robot, Bioinspired, Modeling, Super-Selective Intra-Arterial Cerebral Infusion (SSIACI), Chemotherapeutic Delivery, Tumor.

## Introduction

The ability to provide safe, minimally invasive access to delicate anatomy deep within the body offers the possibility for improved diagnosis and targeted therapy[1]. This is highly apparent in the case of super-selective intra-arterial cerebral infusion (SSIACI), which is a treatment approach for cerebral tumors involving catheter-based delivery of chemotherapeutic agents into the tumor's capillary network for highly localized vascular uptake[2]. Despite numerous advantages of SSIACI over traditional intra-arterial delivery, including reduced systemic toxicity and higher localized dosage delivery, navigation of passive cerebral catheters suffers from intra-operative challenges including cognitive strain on the operating surgeon and a subsequent risk of tissue penetration[2,3]. To improve upon manual navigation of passive guidewires and catheters, soft continuum robotic designs have been proposed which utilize a range of actuation methods including pneumatics[4], hydraulics[5], tendon-driven[6], smart material alloys[7] and magnetics[8]. Of these, magnetic actuation has presented a promising miniaturized approach with potential for arbitrary design variation to suit a range of applications[9]. Magnetic soft continuum robots (MSCRs) are deflected using magnetic forces and torques, produced via interactions between externally generated actuating magnetic fields and magnetically active regions embedded within their soft structures[10,11] Wireless actuation enables miniature designs with high dexterity which has led to numerous MSCR developments for endoluminal applications. These include: closed-loop shape-forming within the bronchial tree[12], targeted laser delivery for ablative lung cancer[13] and cardiac [14], or reconstructive cartilage therapy[15] and grasping and retrieval tasks in the gastrointestinal tract[16].

The majority of MSCRs to date have focused on uniform cylindrical geometries with either a single fixed magnetic tip segment[17] or a distribution of variable magnetic properties over a larger robot length[9,18,19]. These approaches are often constrained to moderate deflections (<90°), as achieving higher actuation angles can be limited by the combination of required magnetic field conditions and low torsional stiffness resulting in undesired twisting instead of additional bending[20]. Mitigation strategies have been proposed through incorporation of stiffening fibers[20] braided backbones[21], or helical geometric designs[22-23] to improve stability. However, the design and fabrication complexity of these approaches sacrifices miniaturization potential whilst limiting the ability to integrate functional components[24]. Creating MSCRs that deliver miniaturized low-stiffness geometries, offer stable high-angle deflections and allow for integration of clinically relevant functionality has yet to be explored and may offer solutions for complex and delicate applications such as SSIACI (Figure 1).

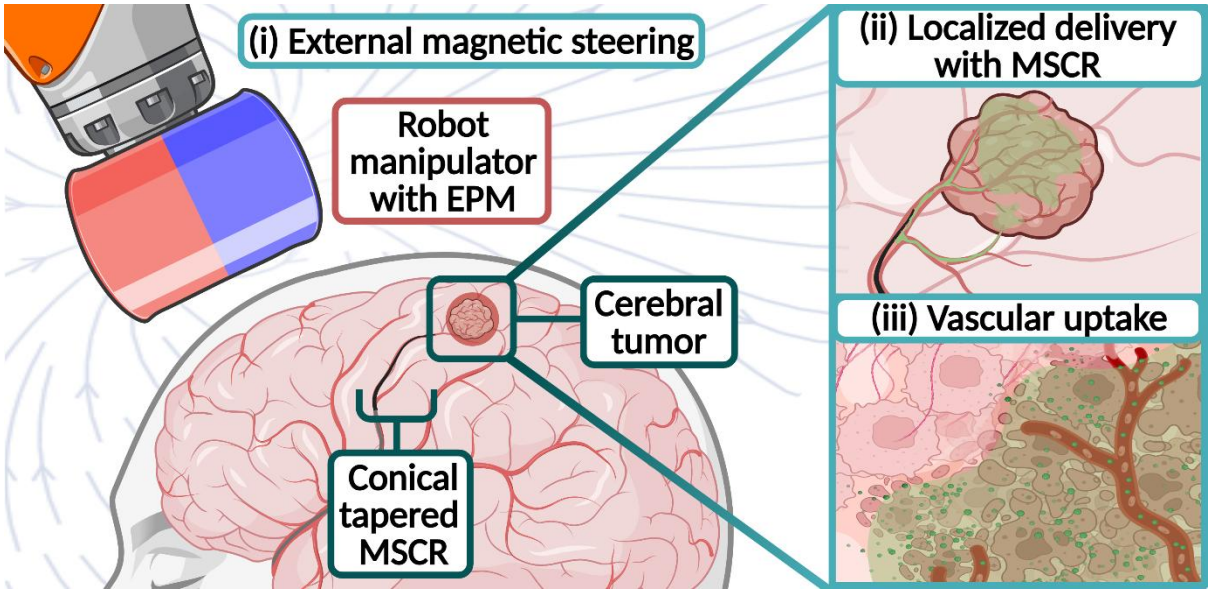


***FIG. 1.*** *Conical tapered MSCR with embedded fluidic microchannels for localized chemotherapeutic delivery in SSIACI. The C-MSCR facilitates (i) magnetically controlled navigation to the tumor's vascular bed, guided by a robot manipulator with an external permanent magnet (EPM), (ii) selective drug release (green) into local tumor vasculature for (iii) uptake into the tumor with minimal drug exposure in surrounding healthy tissue.* ***Created in BioRender. Bacchetti, A. (2025) https://BioRender.com/xn53efu***

In the presented work, we introduce a conical tapered MSCR design (C-MSCR) to enable enhanced low-field deflections, stable high-angle actuation and integration of fluidic microchannels (μ-channels) suited to the navigation and therapeutic delivery challenges associated with SSIACI. We evaluate the influence of the C-MSCR's octopus-inspired geometry on deflection performance for axially magnetized designs of ≤2 mm diameter through discretized analytical modeling, finite element simulation (FEM), Material Point Method (MPM) simulation and experimental evaluation. The retained monolithic structure further enables integration of embedded axial and lateral fluidic μ-channels to illustrate the clinical potential of C-MSCRs in magnetically guided SSIACI. We demonstrate the ability of C-MSCRs to navigate within a neurovascular tumor phantom under external magnetic fields for selective drug simulant delivery under pulsatile flow conditions.

## Tapered Magnetic Soft Continuum Robot Design and Modelling

Conical tapering of the MSCR's geometry implies a continuous variation in cross-section as a function of length. For the proposed C-MSCR designs (Figure 2A), we consider tapers with a linear reduction in diameter between the proximal and distal end. The dimensions of the C-MSCR can therefore be defined by the proximal base diameter ($d_p$) and the reduction (or proximal-distal) ratio ($\eta$), where $\eta = d_p/d_d$ and $d_d$ is the distal tip diameter. We consider designs with a fixed proximal diameter of $d_p = 2$ mm, a length ($L$) of 50 mm, and discrete reduction ratios of: $\eta = 1$ (0% diameter reduction with respect to $d_p$, giving $d_d$ = 2 mm); $\eta$ = 1.5 (33.50% reduction, $d_d$ = 1.34 mm); $\eta$ = 2 (50% reduction, $d_d$ = 1 mm); $\eta$ = 2.5 (60% reduction, $d_d$ = 0.80 mm); and $\eta$ = 3 (67% reduction, $d_d$ = 0.66 mm).

The proximal base diameter ($d_p$) was selected to allow for C-MSCR integration onto a 2 mm diameter catheter for endovascular insertion and for integration of fluid delivery µ-channels. Compared to cylindrical geometry, tapering within the structure will alter both the bending stiffness and magnetic torque as a function of the robot's arc length, $s$, thus impacting the resulting deflection behaviour under actuating fields. For cylindrical MSCR geometry under homogeneous magnetic fields, analytical models based on Euler-Bernoulli beam deflection assumptions have been developed[25], relating the magnetically induced internal bending moment, $M_b$, to the robot's curvature $\kappa$, as

$$M_b = EI\kappa \tag{1}$$

where *E* is the robot's Young's Modulus and *I* is the area moment of inertia about the bending axis. Magnetically induced torque will occur due to the dipole moment $\boldsymbol{M}$ of the axially magnetized MSCR being within a homogeneous magnetic field, $\boldsymbol{B}$, expressed as

$$\boldsymbol{M_b} = \boldsymbol{M} \times \boldsymbol{B}. \tag{2}$$

For in-plane bending under an orthogonal applied field, this may be expressed as

$$\frac{EI}{A}\kappa = |\boldsymbol{M}||\boldsymbol{B}|\sin\left(\theta_L - \frac{\pi}{2}\right) \tag{3}$$

Where $A$ is the cross-sectional area of the MSCR and $\theta_L$ represents the rotation angle at the tip with respect to the unactuated axial direction of the MSCR (X-axis in our convention). However, for the case of a conical taper, the values of $I, A$ and $|\boldsymbol{M}|$ are all dependent on the position along the MSCR, as the radius $r$ reduces along its arc length, $s$, as

$$d_{CS}(s) = d_p + \left(\frac{d_p}{\eta} - d_p\right)\frac{s}{L}, \quad r(s) = \frac{d_{CS}(s)}{2} \tag{4}$$

where $d_{cs}(s)$ is the local cross-sectional diameter at distance s along the MSCR. The area moment of inertia $I(s)$ and area $A$(s) become

$$I(s) = \frac{\pi}{4}r(s)^4, \quad A(s) = \pi r(s)^2 \tag{5}$$

respectively. Therefore, the bending stiffness of the C-MSCR, $K_b(s)$, and local magnetically induced bending moment, $\boldsymbol{M_b}(\boldsymbol{s})$ vary at differing rates over the robot's length. To account for this, we consider the suitability of alternative modelling approaches for capturing the

bending behaviour of the C-MSCR, in the form of an analytical discretized elastic model, an FEM model, and an MPM simulation.

The following material and magnetic assumptions were applied to all models: Young's modulus $E$ = 105 kPa[26], magnetic remanence $m_a$ = 120 kAm$^{-1}$ [26] and non-deflected C-MSCR length L = 50 mm. A homogeneous material design was adopted with the integrated μ-channels assumed to have a negligible effect on deflection. In all simulations, the applied orthogonal magnetic field was increased between 0 - 5 mT in 0.50 mT increments, and 0-15 mT in 2.50 mT increments. Gravitational forces were assumed to be small in comparison to applied magnetic forces and were thus ignored, such that C-MSCR deflection considered only the applied magnetic torques and restoring elastic torques.

## *Discrete Elastic Model*

For a tapered beam under uniform loading, a virtual discretization approach may be taken to iteratively determine bending stiffness, magnetic moment and thus loading effects across its cross-sectional diameter[27]. We assume elastic bending deformation and negligible axial extension/shrinkage under actuation. The C-MSCR is idealized as being divided along its length into $N$ sub-elements of length $ds$, as

$$ds = \frac{L}{N}, \tag{6}$$

with each having a constant cross-section with uniform area moment of inertia and cross-sectional area determined from (5), where $s = ids$ and $0<i<N$. The stiffness of each segment $K_{b_i}$can be calculated as

$$K_{b_i} = \frac{EI_i}{ds}. \tag{7}$$

For each segment, the associated deflection angle $\theta_i$ induced by magnetic torque $\boldsymbol{M_{b_i}}$ may be determined as[28]

$$\theta_i = k_{b_i}^{-1} \boldsymbol{z}_i^T \boldsymbol{M_{b_i}} \tag{8}$$

where $\boldsymbol{M_{bi}}$ is determined based on the local magnetic volume and relative orientation with respect to the applied field, as in (2). The orientation of the end of segment $i$ may be described with respect to its base $\mathbf{O_i}$ by a rotation of $\phi_i$ around the basis unit vector $\boldsymbol{e}_{zi}$ of the principal axes of frame $\mathbf{O_i}$ as

$$\boldsymbol{D}_i = e^{\boldsymbol{e}_{zi}\theta_i} \tag{9}$$

and the position of the end of successive segments, as

$$\mathbf{O_{i+1}} = \mathbf{O_i} + \boldsymbol{D}_i ds \boldsymbol{e}_{xi}. \tag{10}$$

Therefore, the orientation and position of any sub-element of the deformed robot, including the distal tip, may be iteratively computed between $0<i<N$ as

$$^{0}\boldsymbol{R}_{i} = \prod_{k=0}^{i-1} {}^{k}\boldsymbol{R}_{k+1} \quad \text{where} \quad {}^{i-1}\boldsymbol{R}_{i} = \boldsymbol{D}_{i} \tag{11}$$

$$^{(0)}\mathbf{O}_{i} = \sum_{k=0}^{i-1} {}^{0}\boldsymbol{R}_{k}{}^{(k)}\mathbf{O}_{k+1} \quad \text{where } \mathbf{O}_{1} = \mathbf{0} \tag{12}$$

The above model was implemented in MATLAB 2023b (Mathworks, Massachusetts, USA) to evaluate tip deflection as a function of taper angle. This utilized piecewise geometric discretization[27-29] for representation of linear geometric and material variation. The modelled C-MSCR consisted of 20 discrete domains ($N$=20).

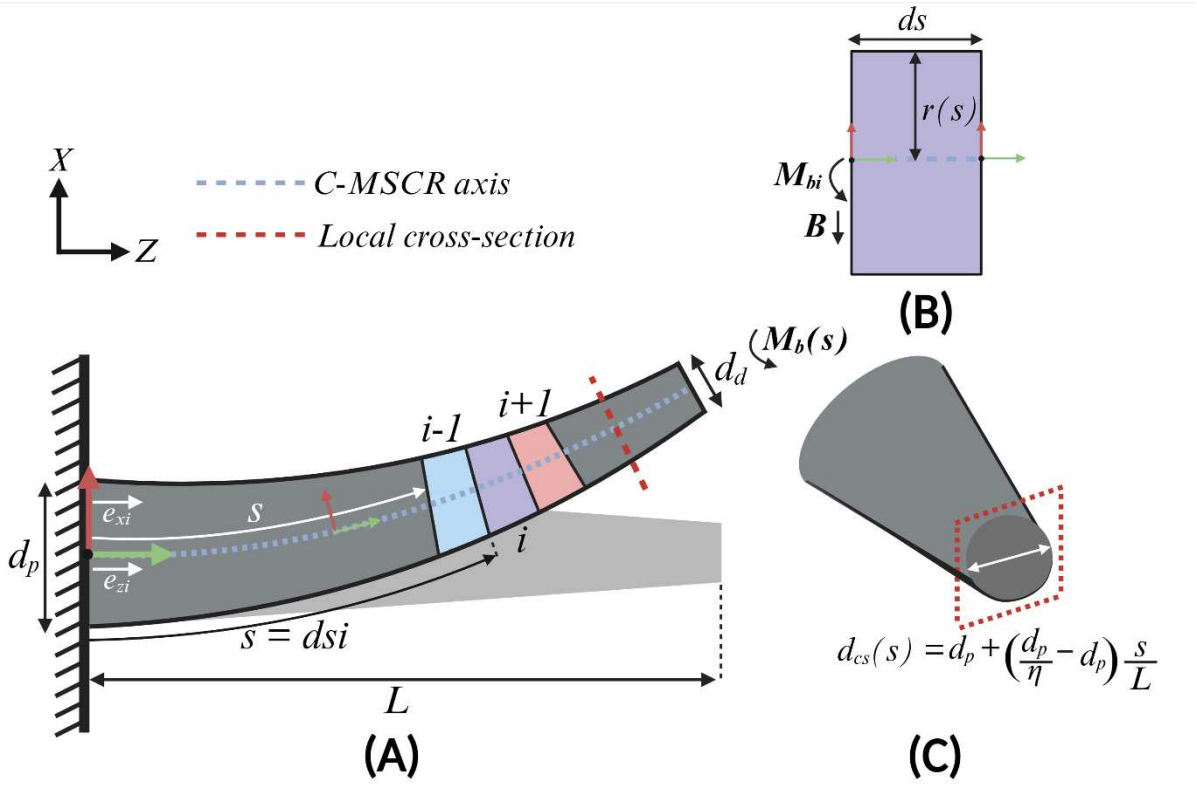


***FIG. 2.*** *Overview of geometrical, loading and deflection conditions for a C-MSCR design with a linear proximal-distal diameter reduction under a magnetic bending moment[27,28,30], (A) simplified global and discrete representation of C-MSCR loading conditions and subsequent deflection, (B) discrete element under loading conditions with negligible axial shrinkage, (C) distal cross-sectional view with C-MSCR cross-sectional diameter.* ***Created in BioRender. Bacchetti, A. (2025) https://BioRender.com/h7bhyl5***

### *Finite Element Model*

For model comparison, an FEM simulation was constructed under the two-dimensional plane strain assumption in COMSOL Multiphysics Suite v5.5 (COMSOL AB, Stockholm, Sweden). **This assumption significantly reduces computational complexity while capturing the dominant in-plane mechanical behavior of the C-MSCR[20]. We therefore neglect out-of-plane effects (secondary bending about the X-axis and torsion about the Z-axis) which are thus assumed to be zero, consistent with the cross-product calculation in Equation (2).** The model employed the solid mechanics and moving mesh modules with Newton-Raphson convergence. The magnetic torque was iteratively calculated as a function of local frame deformation angle and imparted via four embedded rigid domains, dispersed evenly along the C-MSCR's length[20]. The free triangular mesh was autogenerated subject to a maximum element size of 0.20 mm and a maximum element growth rate of 1.1. The resultant model was comprised of 8200 finite triangular elements.

### *Material Point Method Simulation*

For comparison with a more general time-dependent simulation suited to capturing soft material interactions, the C-MSCR design was also modelled with a mesh-free MPM software. The MPM utilizes a neo-Hookean hyperelastic material model and represents soft continuous geometry through a combination of particle-based representation and a fixed grid model. Simulation parameters were configured to $5x10^2$ particles per $mm^3$, grid spacing of 1 mm, simulation time step of $4 \times 10^{-5}$ s, and applied damping coefficient of 200 $s^{-1}$ [31].

## C-MSCR Fabrication and Experimental Characterization

Conical taper designs were fabricated using low-pressure injection molding (Figure 3A). Reconfigurable injection mold cases were 3D printed (PLA, Ultimaker S5, The Netherlands) for the taper ratios $\eta \in \{1, 1.50, 2, 2.50, 3\}$. **Ecoflex 00-30 silicone (Smooth-On Inc., Pennsylvania, USA) was selected as a two-part prepolymer with low viscosity and high mixability with particulates including magnetic neodymium-iron-boron (MQFPB+,Magnequench GmbH, Germany), in comparison with other curable silicone agents [26]. This allowed for feasible manual injection molding and demolding of submillimeter-scale tapered tips. Furthermore, numerous recent contributions have reported using magnetically doped Ecoflex 00-30 for MSCRs with significant magnetic deflection and reliable simulation across different modelling approaches[25,31,32]. We therefore selected Ecoflex 00-30 for C-MSCR fabrication and modeling with embedded NdFeB particulars.** Silicone and neodymium-iron-boron (NdFeB) microparticles were mixed in a 1:1 mass ratio and degassed in a high-vacuum mixer at 1400 rpm, 20 kPa for 90 seconds, and then injected into the cases. All samples were cured at 40 °C for 20 minutes and subsequently exposed to an axial impulse field of >4 T (IM-10- 30; ASC Scientific, Rhode Island, USA) whilst constrained within the original mold case to impart axial magnetization. A series of white tracking markers were placed at 5 mm distances along the MSCR length to aid in visual deflection analysis.

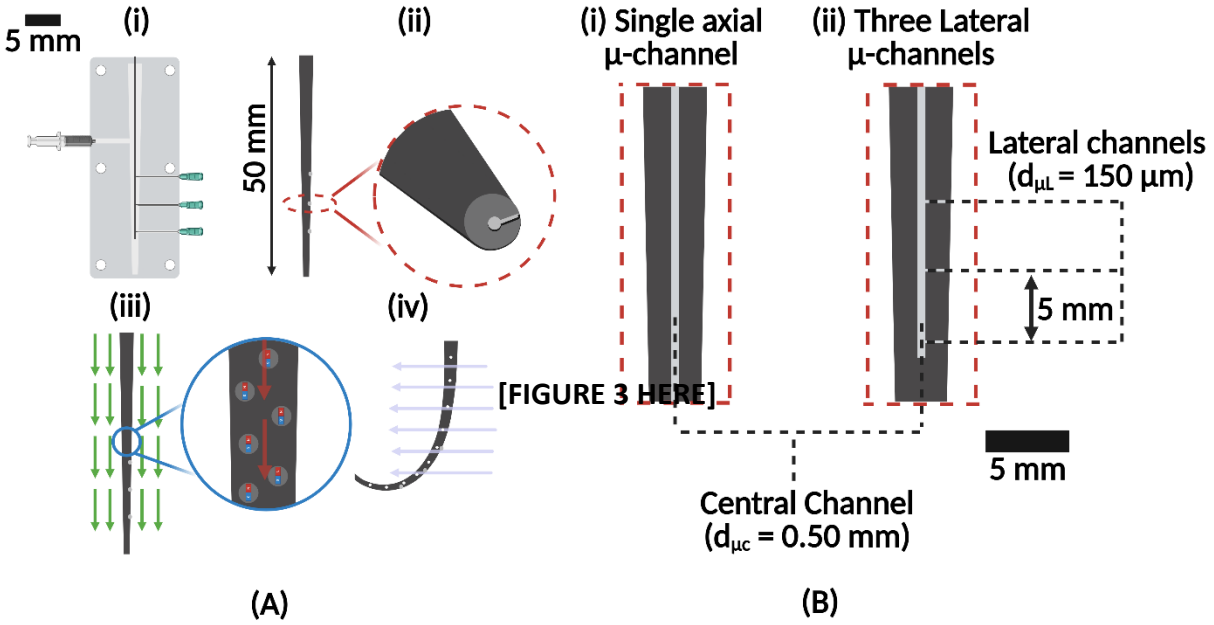


***FIG. 3.*** *C-MSCR design and fabrication for characterization and adaptation to low-diameter SSIACI, highlighting (A) general fabrication procedure: (i) magnetic silicone paste (NdFeB + EcoFlex-0030) cured in a reconfigurable injection molding case with removable embedded nitinol rods for μ-channel creation, (ii) cross sectional C-MSCR schematic with a single lateral μ-channel (iii) axial magnetization (red arrows) imparted after exposing C-MSCR to a saturating magnetic field of >4 T (green arrows), and (iv) C-MSCR actuated under controlled magnetic field conditions, with white markers for visual tracking, (B) cross-section of C-MSCR midpoint with channel configurations, (i) single axial channel for tip-based delivery, (ii) three lateral μ-channels connected to a central axial channel for lateral delivery.* ***Created in BioRender. Bacchetti, A. (2025) https://BioRender.com/t4lhnmy***

C-MSCR actuation performance was evaluated through exposure to a range of homogeneous applied magnetic fields. Designs were mounted vertically within a three-dimensional Helmholtz coil (3DXHC12.5-300), Dexing Magnet Tech. Co., Ltd. Xiamen, China), and exposed to uniform magnetic fields of up to 15 mT (Supplementary Figure 1). A camera (acA2040-120uc Basler AG) was positioned perpendicular to the primary bending plane and used to record quasi-static deflections of the MSCR at each applied field. White markers (at nine discrete points along the C-MSCR's length) were isolated in each deflection profile and utilized to identify deflection in X (horizontal) and Z (vertical) directions, as well as deflection angle at nine discrete points along the C-MSCR's length. Markers were separated by 5 mm distances. For a specified marker, deflection angle was measured as the angle swept between two deflection states and relative to a local tangential reference. This was determined on ImageJ analysis software (National Institutes of Health, Maryland, USA). Camera calibration and correction from potential lens shape defects was completed using a MATLAB 2023b Image Undistortion package (Mathworks, Massachusetts, USA). For model-based comparison, all deflection profiles were either reconstructed through extraction of centreline deflections in

experimental and MPM methods, or through visual reconstruction from centreline point deflections in discretized and FEM-based modeling.

Characterization experiments were performed under: (1) coarse high field conditions with orthogonal magnetic fields of 0-15 mT applied in increments of 2.50 mT, and (2) refined low field conditions with orthogonal magnetic fields of 0-5 mT in increments of 0.50 mT. Three repeat tests were conducted for each sample-field combination, and C-MSCRs were allowed to settle for 10s at each applied field before imaging. To evaluate the potential of C-MSCRs for high-angle deflections (>90°), cylindrical and high taper designs ($\eta = 1$ and $\eta = 2$ respectively) were subjected to a 10 mT homogeneous magnetic field with increasing rotation angle in the MSCR's primary bending plane. A textured paper backboard was used to promote in-plane tip deflection throughout higher angle deflections and restricted the MSCRs from out-of-plane motion as extreme field angles (>180°) were approached. Angular magnetic field direction with respect to the X-axis ($\gamma$) was altered between 0° and 320°, in 10° increments while measuring tip deflection angles. Workspace along the C-MSCR's length was determined visually by tracking the deflection of all nine white markers under the specified field conditions.

**Furthermore, we analyzed and compared oscillatory tip displacements of a cylindrical ($\eta$ = 1) and tapered catheter ($\eta$ = 3) under various cerebral artery flow conditions. To achieve pulsatile flow conditions, a FlowBox One pulsatile flow machine (HumanX Medical Simulators, Florida, USA) supplied a translucent blood simulant to a transparent flask. This was prepared by mixing distilled water and glycerol (Sigma Aldrich, Missouri, USA) in a 60:40 volume percentage ratio under controlled heated conditions[33]. This produced a fluid with an approximate viscosity at room temperature of 4.0±0.40 ×10$^{-3}$ Pa.s and density of 1.050±0.050 ×10$^{3}$ kgm$^{-3}$, closely replicating those of blood[34]. The pulsatile machine pumped fluid at approximately 60 beats per minute. Each catheter was placed at an outlet pipe from the machine and aligned axially along the pulsatile flow path, representing its nominal configuration during intravascular navigation. Catheter oscillation was compared under three flow conditions, selected in accordance with three vessels which are commonly navigated throughout SSIACI. Each vessel flow condition was characterized through flow rate (FR) and mean arterial pressure (MAP), which were then imparted by the FlowBox One. Selected vessels included the interior carotid artery (ICA), middle cerebral artery (MCA) and anterior cerebral artery (ACA). Vessel flow conditions were applied as follows: ICA FR = 4.21 mls$^{-1}$, MAP = 70 mmHg, MCA: FR = 2.40 mls$^{-1}$, MAP = 62 mmHg, and ACA: FR = 1.33 mls$^{-1}$, MAP = 70 mmHg[35-38]. For both catheters, we recorded videos of their oscillations (25 frames per second) and post-processed the frames over a 10-second period to track tip positions (Computer Vision Toolbox, MATLAB 2023b, Mathworks, Massachusetts, USA). To compare the influence of taper and vessel flow conditions, the horizontal displacement was determined in each case with respect to the mean of the data; assumed as the approximate center of the oscillation. Comparison was additionally made through calculation of the standard deviation in each case.**

## *Deflection Characterization under Orthogonal Magnetic Fields*

Figure 4 shows the progression of tip deflection angle as a function of applied orthogonal magnetic field strength for various C-MSCR designs (Supplementary Video 1 and Supplementary Video 2). Image overlays of C-MSCR deflections are presented for low-field

and high-field ranges (Figure 4A). For high field strength actuation, all taper ratios approached maximum tip deflection angles close to that of the applied field angle (86.96° - 90.81°). However, for higher taper ratios, this asymptote is approached more rapidly, highlighting a mean difference of 9.81° between the $\eta$ = 1 and $\eta$ = 3 designs. The influence of taper geometry is more apparent within the low-field region, where the $\eta$ = 3 design observes 16.47° higher deflection on average across the entire field range. Upper and lower deflection measurement errors are reported for all experimental repeats (Figure 4B and Figure 4C).

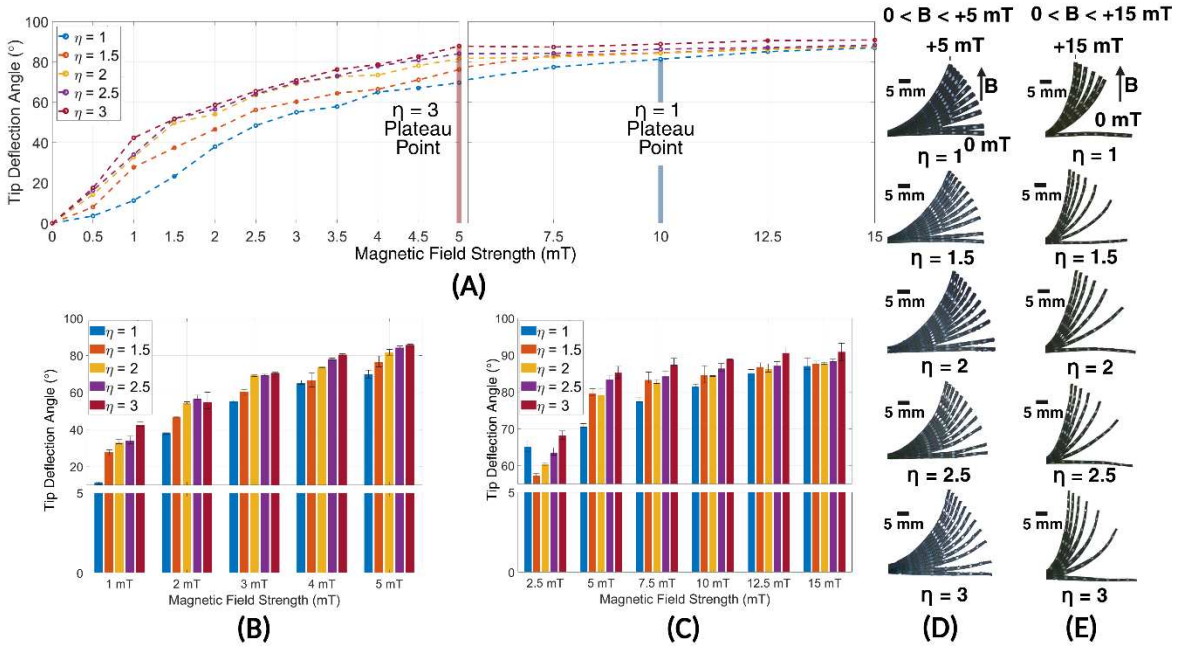


***FIG. 4.*** *Comparison of tip deflection angle for varied C-MSCR designs under low (0 - 5 mT) and high strength (0 – 15 mT) uniform orthogonal magnetic field conditions, (A) summary of tip angle deflection responses across low and high field strength ranges for η = 1 (blue), η = 1.5 (orange), η = 2 (yellow), η = 2.5 (purple) and η = 3 (maroon), with an intermediate break at 5 mT, (B) comparison of tip deflection angles at selected applied field between (B) 0-5 mT, and (C) 0-15 mT, with upper and lower measurement error bars shown. Images of MSCR deflections shown between (D) 0-5 mT, (E) 0-15 mT.* ***Created in BioRender. Bacchetti, A. (2025) https://BioRender.com/gkldpuu***

## C-MSCR Model Comparison

Considering the influence of the most extreme taper, we present modeling results $\eta = 3$ design under uniform field conditions (Figure 5). For the 0-5 mT range, RMS errors across the field range are 14.13°, 7.23° and 5.28° for discretized, FEM and MPM respectively. For the 0-15 mT range, RMS errors are 8.45°, 4.55° and 2.74° for discretized, COMSOL and MPM, respectively.

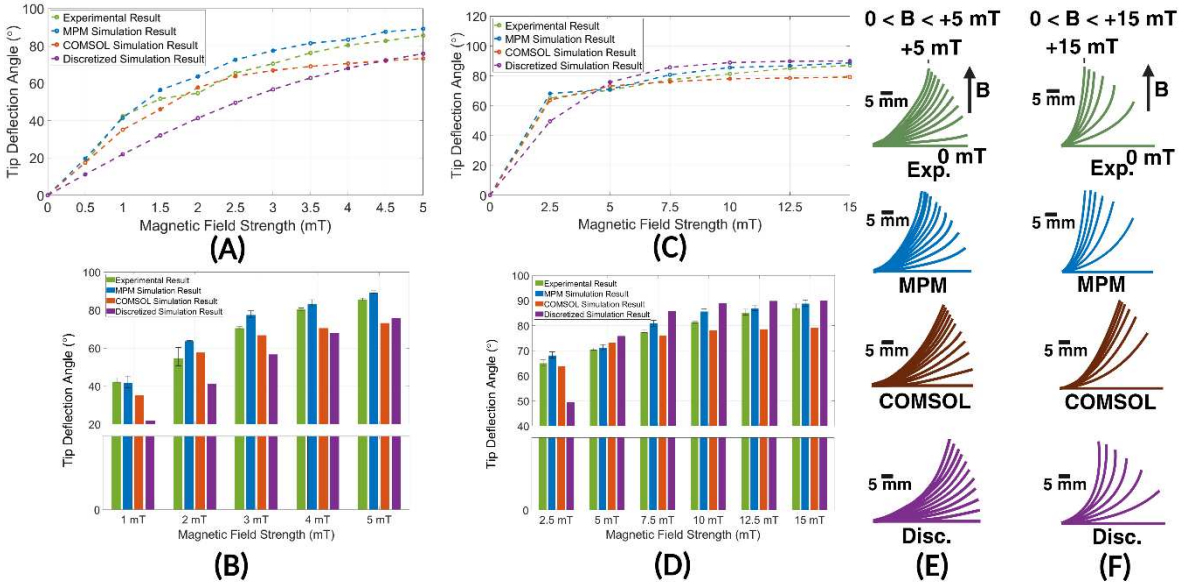


***FIG. 5.*** *Comparison of model and experimental tip deflection angle responses for cylindrical and C-MSCRs under low (0 - 5 mT) and high strength (0 – 15 mT) uniform field conditions. Error bars are presented for experimental and MPM outputs. Includes responses for experimental (green), MPM (blue), COMSOL (orange) and discretized (purple) methods, (A) tip deflection angle responses between 0-5 mT, (B) tip deflection angle responses between 0-15 mT, (C) comparison of tip deflection angle between 0-5 mT in 1 mT increments, with upper and lower measurement error bars, (D) comparison of tip deflection angle between 0-15 mT in 2.50 mT increments, with upper and lower measurement error bars strength deflection profiles, (E) experimental and model-based deflection profiles between 0-5 mT, (F) experimental and model-based deflection profiles between 0-5 mT.* ***Created in BioRender. Bacchetti, A. (2025) https://BioRender.com/eadpcqr***

## *Deflection under High-Angle Fields*

Figure 6 highlights the deflection and workspace potential of higher ratio tapered designs under angled magnetic fields. A design with $\eta = 2$ was selected as it represented the maximum feasible taper with sufficient backboard contact to mitigate out-of-plane tip deflection under high-angle fields. We report and distinguish the linear relationships between magnetic field angle ($\gamma$) and tip deflection angle ($\theta$) at extreme field angles (>90°) and highlight the influence of tapered geometry on achievable workspace under high-angle deflections (Supplementary Video 3).

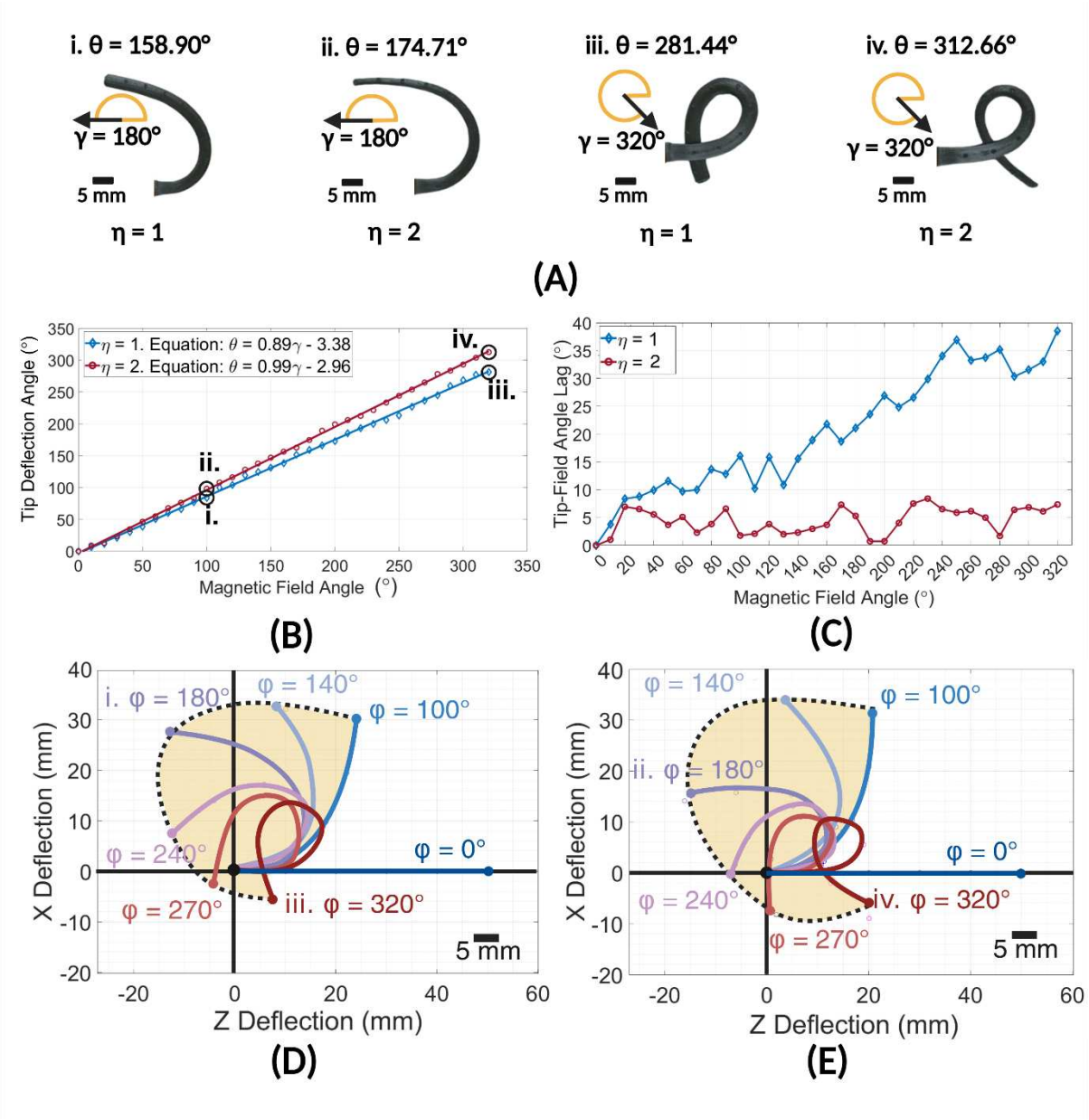


***FIG. 6.*** *Tip deflection, workspace and deflection profiles for cylindrical and C-MSCR designs under high-angle rotating fields, (A) η = 1 and η = 2 MSCR deflection profiles under rotating 10 mT field angles between 0° - 320°, highlighting: (i) η = 1, γ = 180° field. ii. η = 2 deflection under a 100° field. iii. η = 2 deflection under a 320° field and iv. η = 2 deflection under a 320° field, (B) comparison of tip deflection angle between η = 1 and η = 2 designs between 0° - 320°, (C) Comparison of tip-field lag between both designs. Observation of lag between each design's tip deflection angle (θ) and the field angle (γ) indicated the degree of tip responsiveness and feasibility to overcome elastic restoring forces throughout extreme deflection, (D) η = 1 tip workspace under between 0 - 320° field angles, (E) η = 2 tip workspace 0 - 320° field angles.* ***Created in BioRender. Bacchetti, A. (2026) https://BioRender.com/mkycko2***

*Passive Catheter Oscillation under Pulsatile Flow*

**We also present a comparison of oscillatory tip displacement for cylindrical ($\eta$ = 1) and tapered ($\eta$ = 3) catheters under ICA, MCA and ACA vessel flow conditions (Figure 7A). Figure 7B highlights the influence of higher taper ratios on a catheter's sensitivity to pulsatile flow. The $\eta$ = 3 design showed a >500 % higher oscillatory tip displacement (maximum = 5.60 mm and standard deviation = 1.90 mm) in comparison to an $\eta$ = 1 design (maximum = 1.20 mm and standard deviation = 0.30 mm), under ACA flow conditions. This was also observed under MCA and ICA conditions, with an increase of 233 % and 53 % under respective vessel flow (Supplementary Video 4).**

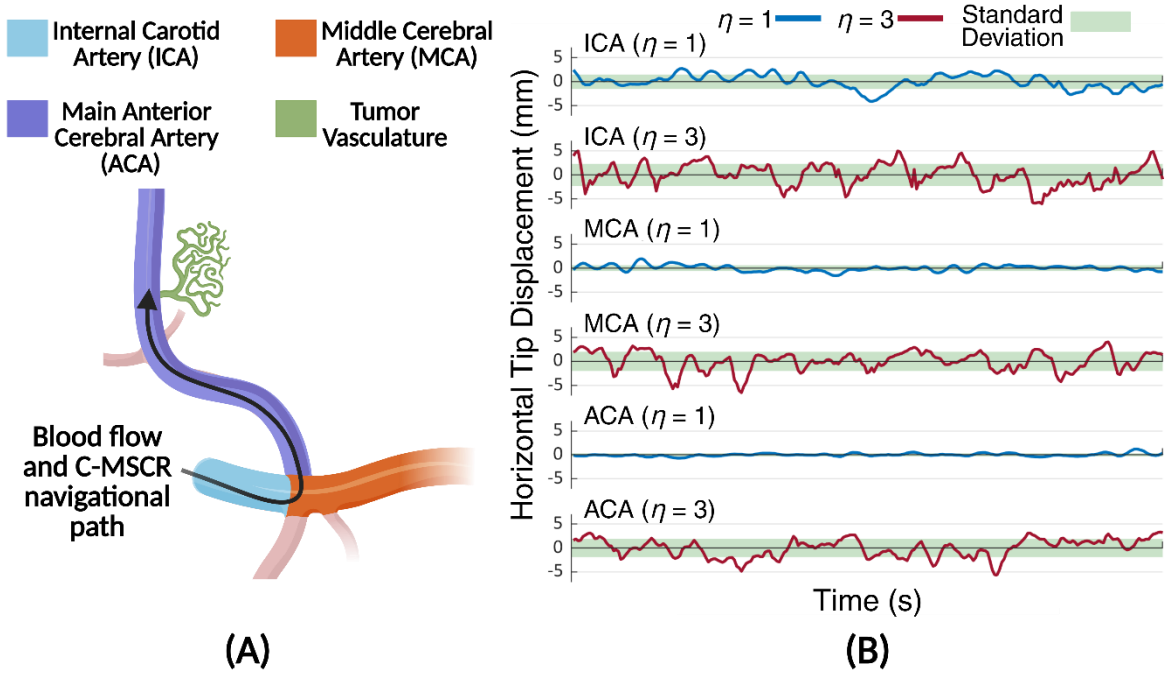


***FIG 7. Comparison of horizontal oscillatory tip displacement for η = 1 and η = 3 designs under ICA, MCA and ACA pulsatile flow conditions. (A) Labelled diagram of blood flow direction and cerebral vessels navigated throughout SSIACI, (B) Horizontal oscillatory tip displacements for η = 1 (blue) and η = 3 (maroon) designs with associated standard deviations (green shading), under respective vessel flow conditions. Created in BioRender. Bacchetti, A. (2026) https://BioRender.com/qhaeyeq***

## *Discussion of Deflection Characterization Results*

As illustrated in Figure 4, the reduced tip stiffness for higher taper designs shows improved tip responsiveness at low fields strengths, with $\eta$ = *3* observing the greatest tip deflections at 0.50

mT (Supplementary Video 1). This trend extends to higher applied 0-15 mT fields (Supplementary Video 2) however the differences are less pronounced as all design approach alignment with the applied field. Comparing experimental C-MSCR deflection behavior to the model predictions (Figure 5) shows good agreement, with all methods capturing the variable curvature and increased tip angle induced by the tapering geometry. The discrete elastic model shows under-prediction at low fields and over prediction at high fields, while the FEM model under-predicts tip deflection in all cases. This is likely caused by the limitation of linear elastic material property assumptions in both cases. Conversely, the MPM accounts for hyper-elastic deformation and thus provided the most accurate representation of a C-MSCR, with only slight over-prediction of tip deflection at high field strengths and RMS errors of 2.74° and 5.28° for 0-5 mT and 0-15 mT ranges respectively. Comparing cylindrical and tapered designs under rotating fields (Figure 6), shows a field-angle-dependent divergence of tip deflection. The C-MSCR with $\eta$ = 2 follows the applied field angle closely over the full range, while the cylindrical MSCR lags behind (**Supplementary Video 3**), as highlighted by the gradients of associated linear expressions for each design (Figure 6B). This resulted in a total reachable workspace for the tapered design, which is approximately 20.87% greater than that of the cylindrical reference.

Overall, the high sensitivity at low field strengths and potential for stable high-angle deflection of higher taper C-MSCR designs may be beneficial in anatomical navigations with limited external magnetic field strengths or highly convoluted anatomy. The tapered design benefits from a 'geometrical anchoring' effect, whereby the majority of MSCR mass at the proximal end (i.e. from the midpoint upwards) remains in a relatively stable deflection, whilst supporting the slender tip to deflect to greater angles, following the applied field. The reduced distal diameter associated with higher tapers also supports navigation into narrow and delicate anatomy, presenting C-MSCRs as suitable candidates for complex catheter operations including selective endoluminal delivery under retrograde flow or navigation throughout high-angle bifurcations.

**Higher taper C-MSCRs generally observe greater oscillatory tip displacement under pulsatile vessel flow (Figure 7B). Across ICA, MCA and ACA flow conditions, the η = 3 design observed 53 %, 233 % and 500 % increases (with respect to the η = 1 case) in horizontal oscillatory tip displacement, respectively. This behavior stems from lower localized stiffness towards and at the catheter's tapered tip. Whilst providing high sensitivity and deflection under low magnetic field strengths, high taper C-MSCRs may commonly observe unstable, oscillatory behavior under arterial flow conditions and in the absence of external fields. This may highlight the need for magnetic stabilization throughout C-MSCR navigation and delivery, achieved through the application and maintenance of a low-strength field to ensure minimal oscillatory behavior in convoluted vasculature. Stabilizing fields may be applied and monitored in conjunction with visual observation and magnetic sensing methods during deployment.**

## C-MSCRs for Targeted Fluidic Delivery

To demonstrate the potential of utilizing C-MSCRs for fluid delivery (in applications such as SSIACI), µ-channel networks were integrated into their monolithic design. A $\eta$ = 3 design was selected to maximize the benefits of the taper and provide the smallest distal tip ($d_d$ = 0.67 mm). Channels were created by placing nitinol rods, ranging between 0.25-50 mm, into the molds at integrated locating points prior to silicone injection (Figure 3A). Two µ-channel configurations were considered: (1) a central axial design for directional tip-based delivery and (2) lateral design with three lateral µ-channels, each with a 5 mm separation distance for radial delivery (Figure 3B). To create the full catheter, a 2 mm flexible PTFE tube was secured to the C-MSCR's proximal base for use in the phantom navigation setup (**Figure 8A** and **Figure 8B**). A 0.25 mm silicone fluid delivery tube was connected directly to the C-MSCR's central µ-channel. The proximal end of the delivery tube was connected to a 10 ml syringe to manually dispense the drug simulant into the design's µ-channel network.

To demonstrate selective delivery under cerebral flow conditions, a neurovascular arterial flow phantom was designed with integrated tumour capillary vasculature (**Figure 8C**). The phantom was based on a segment of the ACA with segments of branching vasculature to healthy peripheral cerebral tissue and a tumor. Anatomical vessel data were extracted from the US National Cancer Imaging Archive[39]. The phantom tumor observed an approximate spherical diameter of 3 cm, with branching vessels to the capillary vasculature ranging between 0.50 – 1.50 mm in diameter. The phantom's main proximal vessel curves through approximately 200°, and must be navigated by the C-MSCR for all delivery scenarios. Additional details of the phantom design and fabrication are presented in Supplementary Text 1.

**To achieve ACA blood flow conditions, the FlowBox One pulsatile flow machine (HumanX Medical Simulators, Florida, USA) was connected to the phantom to supply the blood simulant.** The pulsatile machine pumped fluid at approximately 60 beats per minute with a mean flow rate of 1.33 ml.s$^{-1}$ [35] and mean arterial pressure of **70 mmHg** representing typical ACA blood flow in adult patients[38]. For the drug simulant, a 99.995:0.005 mass ratio of distilled water to fluorescent green dye powder (MOB Cosmetics, London, UK) was utilized. A 395 nm ultraviolet light source (Lepro Innovation Inc., Nevada, USA) was utilized to enhance simulant visibility during testing. A camera (acA2040-120uc Basler AG) was positioned approximately 60 cm above the phantom rig to record navigational and delivery tasks (**Figure 8B**).

### *Phantom Navigation*

The C-MSCR was manually inserted into the phantom's lumen through a circular 2.50 mm diameter port at the rear side of the setup. The insertion port leads directly to the lumen's approximate centerline, where the C-MSCR intercepted pulsatile flow resulting in oscillatory

displacements in the absence of external magnetic fields. The C-MSCR was inserted approximately 14 mm into the phantom without external magnetic control to evaluate this unconstrained oscillation analysis under pulsatile flow. Stabilizing and navigational magnetic fields were subsequently applied at the respective phantom positions (SF, ANF for axial delivery and LNF for lateral delivery) using a single KUKA robot arm with an external permanent magnet (EPM) end effector, situated within 15-20 cm of the phantom (**Figure 8A**). Three custom magnetic field sensors were attached to the phantom platform to measure magnetic field components and subsequent magnetic norm throughout navigation[40].

A challenge which is rarely reported throughout MSCR endoluminal navigation involves the effect of forces (exerted through physiological processes) on the catheter's intra-operative displacement in low-diameter lumen. Here, we assess the effect of endovascular pulsatile flow on catheter tip displacement. Throughout ACA phantom navigation, we utilized the tapered design's tip responsiveness to magnetically stabilize the robot under pulsatile flow and minimize the risk of vessel wall adherence (**Supplementary Video 5**). Throughout each delivery scenario, we navigated the C-MSCR to the respective target site, first under low strength stabilizing fields (4.60 mT with a magnetic norm vector of $\hat{B}_{ANF}$ = [0.27 0.22 0.95]) and then transitioning to higher strength navigational fields (14 mT with a magnetic norm vector of $\hat{B}_{LNF}$ = [-0.51 -0.76 0.41]) at ANF and LNF. **Phantom insertion was manually controlled, with the C-MSCR's position directly viewed by the operators throughout all points of navigation and drug simulant delivery. The magnetic sensors were placed at the base of the phantom's platform to record and track magnetic field strength continuously throughout C-MSCR insertion. The position of the actuating robotic platform was manually adjusted in accordance with both visual and magnetic sensor information**. Oscillatory tip displacement was measured at each key reference point (**Figure 9**) with ImageJ analysis software (National Institutes of Health, Maryland, USA).

### *Simulated Drug Delivery*

Three delivery scenarios were performed: (1) injection at the phantom's inlet to represent traditional intra-arterial delivery, (2) tip-based axial delivery at AD (**Figure 8D**) utilizing a C-MSCR with a single axial channel (3) radial delivery at LD (**Figure 8D**) utilizing a C-MSCR with three lateral µ-channels at approximate 5 mm separation distances. The distal µ-channel was situated at 5 mm from the MSCR's tip. Lateral channel separation distances were selected such that simulant delivery was directly above the tumour vascular bed. In each scenario, 10 ml of drug simulant was delivered in approximate 0.50 ml volumes and synchronized with the diastolic (rest) phase. Delivery was completed over an approximate period of 15-25s.

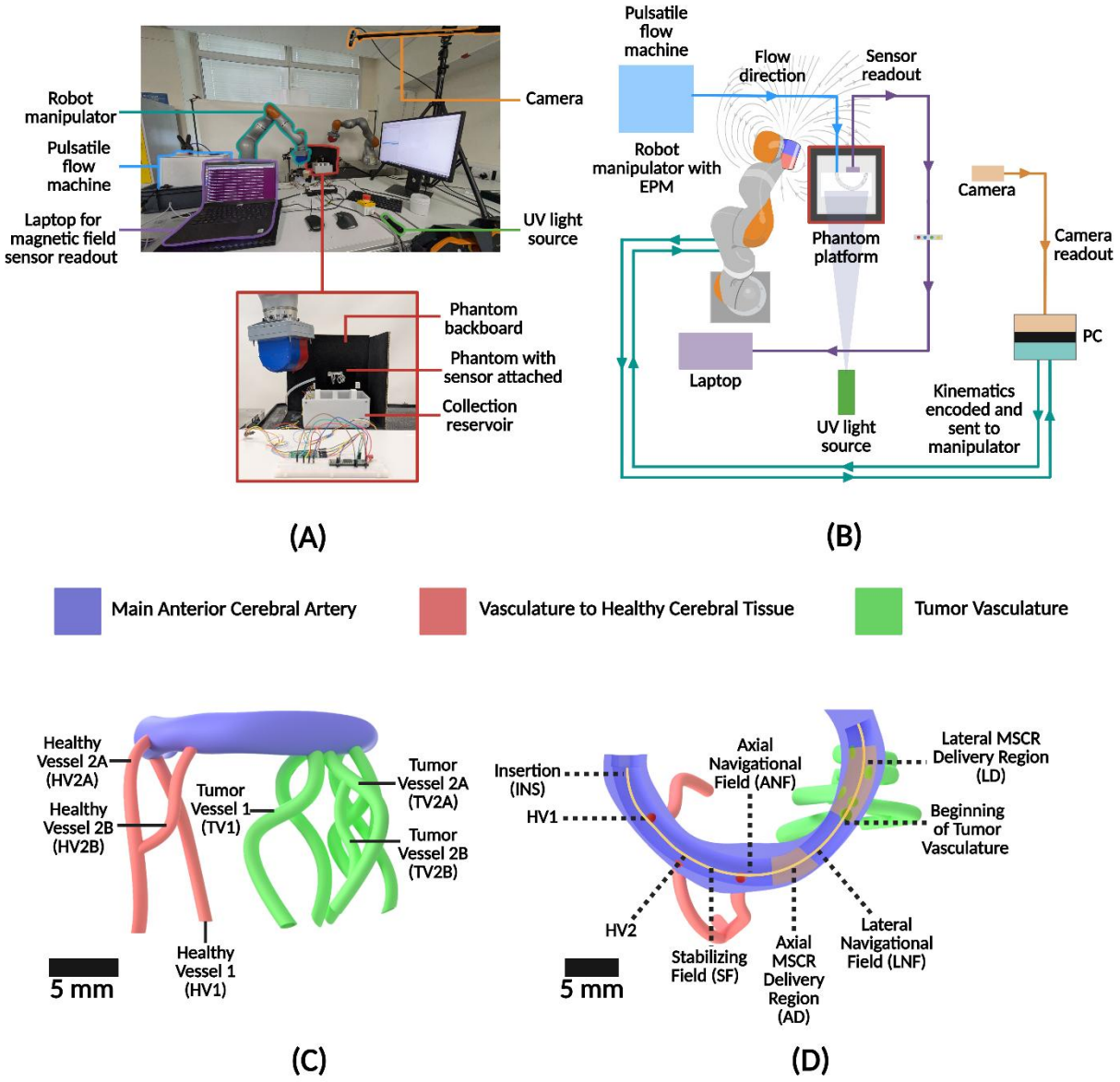


***FIG. 8.*** *Experimental setup and colour coded neurovascular flow phantom, (A) phantom experiment setup with key apparatus with expanded view of phantom rig, (B) systematic diagram highlighting equipment interactions and information flow, (C) phantom diagram of the main ACA vessel (purple) alongside branching vasculature to healthy peripheral cerebral tissue (red) and vasculature supplying a tumor (green), highlights key reference vessels for analysis and comparison of fluorescence intensity throughout traditional intra-arterial, axial and lateral μ-channel delivery, (D) C-MSCR navigational path from insertion to μ-channel delivery, annotated with key reference points for fluorescent intensity, magnetic field application and C-MSCR stabilization throughout navigation and delivery.* ***Created in BioRender. Bacchetti, A. (2026) https://BioRender.com/k47ro9o***

## *Analysis of Navigational Stability*

We obtained characteristic profiles of oscillatory tip displacement for axial and lateral C-MSCR navigation, highlighting significant reductions in displacement upon application of stabilizing and navigational magnetic fields (**Figure 9**).

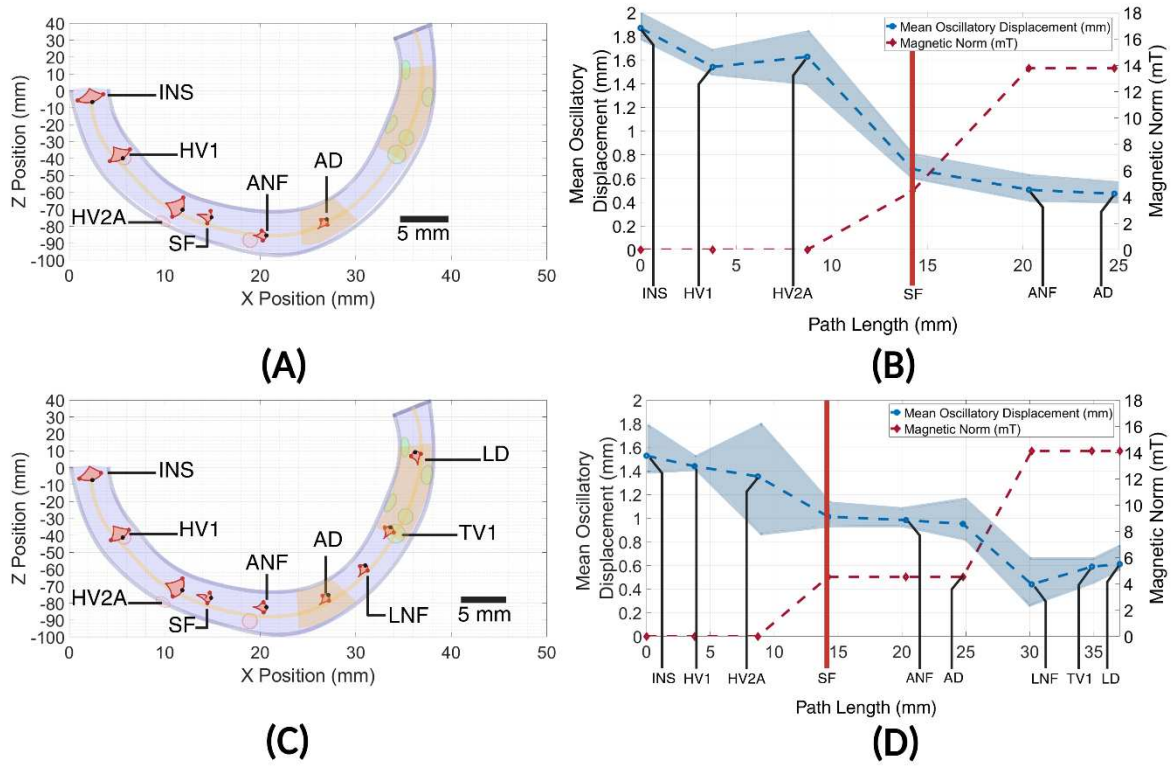


***FIG. 9.*** *Mean oscillatory displacement of axial and lateral C-MSCR tips throughout ACA navigation, stabilizing field (SF) and navigational field positions (ANF and LNF), (A) tracked oscillatory displacements for the axial C-MSCR throughout navigation, with red parabolic 'fans' representing positional tip displacement at each reference point, (B) mean oscillatory displacement against magnetic norm for the axial C-MSCR with shaded error region, (C) tracked oscillatory displacements for the lateral C-MSCR throughout navigation, (D) mean oscillatory displacement against magnetic norm for the lateral C-MSCR, with shaded error region.* ***Created in BioRender. Bacchetti, A. (2026) https://BioRender.com/6ljr4o8***

Navigation between HV1 and HV2A highlighted the greatest risk of vessel wall contact, with displacement fans indicating the narrowest tip-wall proximities of 0.20 mm for both designs. The absence of actuating fields alongside the presence of HV1 and HV2A flow paths caused a tendency to deflect towards a branching healthy vessel. This highlights the possible cause of misguided navigation and treatment delivery with in both low-diameter conventional and SCR catheter designs. Applying the stabilizing field (SF) significantly reduced oscillatory displacement, with axial and lateral designs observing percentage reductions of 58.24% and 61.50% between HV2A and SF respectively. Applying ANF and LNF maintained tip stability and prevented tip-wall contact throughout both synchronized delivery with the axial design and high-angle deflection with the lateral design at TV1.

*Analysis of Drug Simulant Delivery*

We obtained characteristic profiles of normalized fluorescent green intensity against time for intra-arterial injection in axial and lateral C-MSCR delivery cases (**Supplementary Video 5**). Intensities from the fifth delivery and dispersion cycles (synchronized with diastolic and systolic phases respectively) were isolated for visual comparison with traditional injection (**Figure 10**). Intra-arterial injection was delivered continuously over an approximate 15 – 30 s period. Corresponding points are highlighted in each comparative intensity profile (**Figure 10**) alongside mean and maximum intensities for each delivery case. HV2A, TV1 and TV2B vessels were selected for comparison of drug simulant dispersion between intra-arterial injection, axial and lateral μ-channel delivery cases. Normalized green intensity was analyzed in the first 15 s of drug simulant delivery for equal comparison between all delivery scenarios.

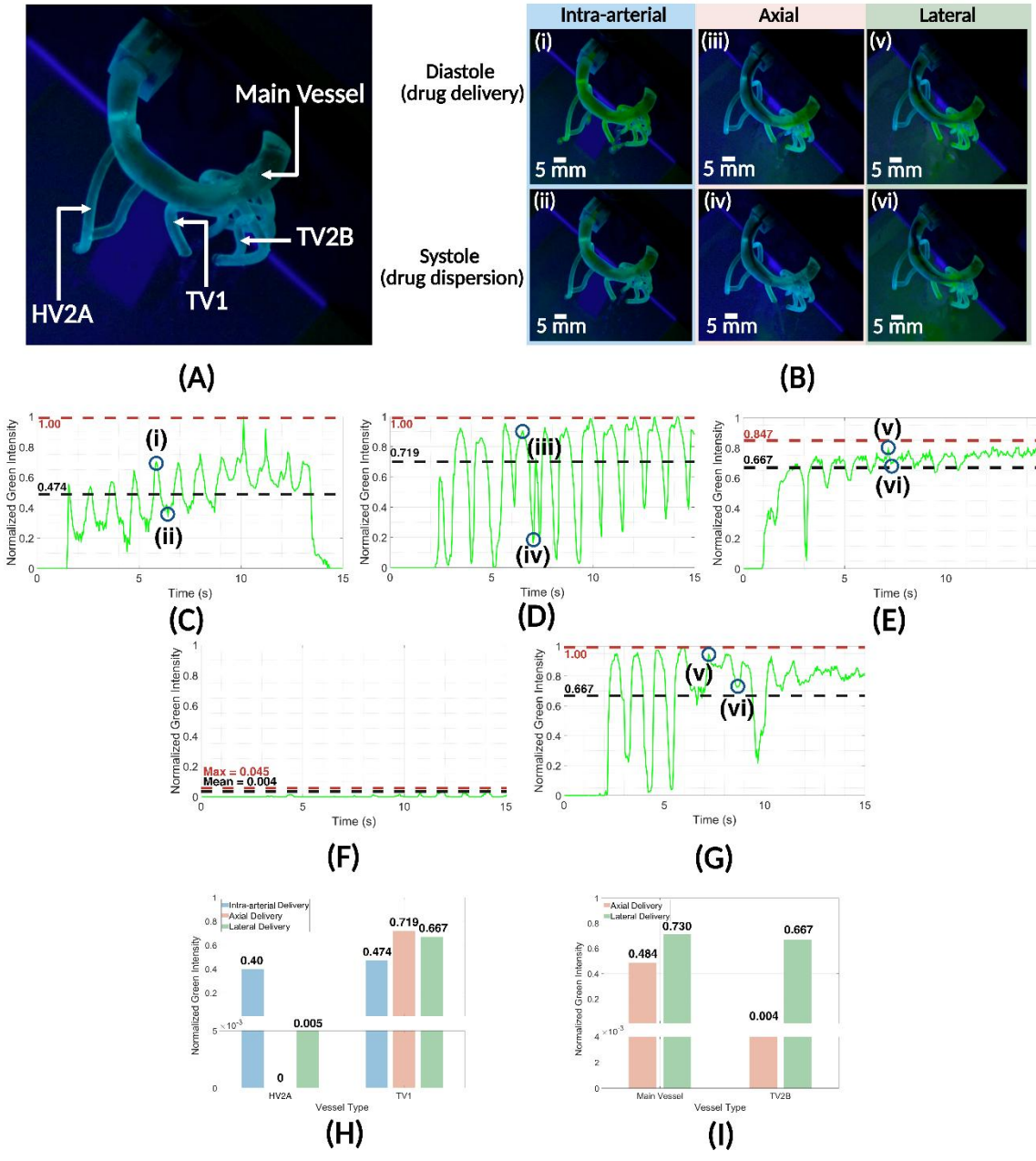

***FIG. 10.*** *Fluorescent distribution profiles, time series and comparative profiles for intra-arterial, axial and lateral C-MSCR delivery cases throughout diastolic and systolic phases, (A) phantom reference with annotated vessels in correspondence with main intensity analysis points throughout delivery, (B) diastolic and systolic fluorescence profiles throughout the fifth delivery pulse. (C) intra-arterial delivery at TV1, (D) axial C-MSCR delivery at TV1, (E) lateral C-MSCR delivery at TV1, (F) axial μ-channel delivery at TV2B, (G) lateral μ-channel delivery at TV2B, (H) comparison of intravenous (blue), axial (peach) and lateral (green) mean intensities in HV2A and TV1 over 15 s, (I) comparison of axial (peach) and lateral (green) mean intensities in the main vessel and TV2B over 15 s.* ***Created in BioRender. Bacchetti, A. (2026) https://BioRender.com/zqz539p***

## *Discussion of Drug Simulant Delivery*

Intra-arterial injection highlighted the general systemic dispersion behavior of traditional chemotherapeutic delivery (**Figure 10C**). This may lead to overexposure of healthy tissue alongside significant reductions in drug uptake and efficacy at the tumor site. Similar mean intensities between HV2A and TV1 (0.40 and 0.474 respectively) were reported, implying equally potent delivery at both sites and potential overexposure of healthy tissue (**Figure 10C** and **Figure 10H**). The axial C-MSCR significantly enhanced capabilities for targeted delivery at the tumor site. At TV1, a mean intensity of 0.719 was reported throughout the 15 s delivery cycle (**Figure 10D**). The C-MSCR's ability to bypass healthy vessels and deliver directly at the opening of tumor vasculature resulted in minimal exposure at HV2A, with a mean value of 0.00 reported for the full delivery cycle (**Figure 10H**). Delivery with the lateral C-MSCR observed a similar profile to the axial delivery case. HV2A exposure was negligible throughout the full delivery cycle, with a mean intensity of 0.004 (**Figure 10H**). The C-MSCR's submillimeter distal tip, alongside optimized lateral microchannel placement allowed for direct delivery above the tumor's vascular bed, with a mean intensity of 0.667 reported at TV1 (**Figure 10E**). In this case, lateral channels were situated outside the lumen diameter and inlet flow path of TV1, which may have resulted in a marginally lower mean intensity in comparison to the axial case (in which the tip's axial channel was situated closest to TV1).

Despite a marginally lower mean intensity throughout lateral delivery, a clear advantage may be drawn with regards to simulant retention throughout systole and dispersion within deeper branching tumour vessels (**Supplementary Video 6**). This was observed through comparison of mean intensities within the main vessel portion above the tumour site and at TV2B (**Figure 10I** and Supplementary Figure 2). In axial delivery, a 'washout' effect from each systolic pulse resulted in the quick removal of simulant from the main vessel and tumor vasculature (**Figure 10F**). Conversely, the lateral C-MSCR required deeper insertion within the main vessel such that μ-channels were situated directly above the tumor's vascular bed. Further insertion disrupted vessel flow conditions, creating a local region of turbulence and lower flow rate around the tumor site, referred to as a 'pooling' effect (**Figure 10G**). Subsequently a sustained, higher-intensity volume of drug simulant remained in the target region between delivery pulses, allowing for greater targeted exposure during systole (trough comparison in **Figure 10F**

and **Figure 10G**). In lateral delivery, average intensities were approximately 161.53% greater in the main vessel above the target tumour, and 89.69% greater in TV1. Lateral delivery also improved delivery in deeper branching vessels, such as TV2B (Supplementary Figure 2), through a combination of increased delivery surface area and drug simulant pooling in the main vessel. Mean intensities in TV2B were reported as 0.004 (**Figure 10F**) and 0.667 (**Figure 10G**) respectively for axial and lateral μ-channel delivery.

## Conclusion

We introduce a bioinspired conical MSCR that enables improved low-field (Figure 4) and high-angle (Figure 6) deflections, and facilitates direct integration of μ-channels to support targeted fluid delivery in diameters of ≤2 mm. Modelling approaches demonstrate the possibility to capture the increased complexity of a lengthwise variation in stiffness and magnetic moment, with MPM showing particularly strong agreement with experimental characterization results (Figure 5). MPM is thus presented as a favourable candidate in the predictive modelling of length-varying geometrical and stiffness in bioinspired MSCRs. In conjunction with digitally driven fabrication, MPM may be a high-potential potential method for the optimization of bioinspired MSCRs (such as the C-MSCR), utilizing anatomical data from the patient to best deliver rapid optimization of geometric, material and magnetic heterogeneity for optimized neurovascular navigation. We demonstrated the potential of C-MSCRs in achieving low-field tip deflections and increased workspace, exceeding the performance of cylindrical designs (**Figure 6**). Lastly, we demonstrate the potential clinical value of these features for atraumatic endovascular interventions such as SSIACI. Through application of magnetic stabilization **for oscillation reduction (Figure 7 and Figure 9),** and steering fields, a C-MSCR with embedded μ-channels was able to navigate through a high-curvature ACA portion under pulsatile flow for the selective delivery of drug simulant to tumor vasculature (**Figure 10, Supplementary Video 5 and Supplementary Video 6**). Future work will seek to expand navigation capabilities to deliver high-angle deflections in patient-specific three-dimensional anatomy by exploiting non-axial lengthwise magnetization profiles and non-linear taper designs. Adapted designs in the form of axial and lateral μ-channels both show improved simulant delivery in tumor vasculature when compared with direct intra-arterial delivery in the major supplying vessel. C-MSCRs therefore provide an extended design space for MSCRs for improved deflection and navigational capabilities, while supporting functional integration of μ-channels for delivering targeted therapy deep within the body.

## Acknowledgments

This work was supported in part by the Engineering and Physical Sciences Research Council (EPSRC) under grants EP/Y037235/1, EP/V047914/1, and EP/V009818/1; the European Research Council (ERC) through the European Union's Horizon 2020 Research and Innovation Programme under grant 818045; and the National Institute for Health and Care Research (NIHR) Leeds Biomedical Research Centre (BRC) (NIHR203331). Any opinions, findings, and conclusions or recommendations expressed in this article are those of the authors and do not necessarily reflect the views of the EPSRC, the ERC or the NIHR. **B. Calmé was supported by the Advanced Research and Innovation Agency (ARIA) under the SMRB-SE01-P01/MORPH grant. J.H. Chandler was supported by the Leverhulme Trust and the Royal Academy of Engineering under the RAEng / Leverhulme Trust Research Fellowships scheme (LTRF-2425-21-154)**

We would like to thank Samwise Wilson, Robyn Flynn and Alfred Alexander for their technical support throughout this project. All figures were produced or modified with Biorender.com. Individual licenses and access links for each figure are provided in the relevant figure caption

## Author Contributions Statement

**Alistair Bacchetti:** Conceptualization (lead), formal analysis (lead), investigation (lead), project administration (lead), validation (lead), visualization (lead), writing – original draft (lead). **Peter Lloyd:** Conceptualization (supporting), methodology (lead), project administration (supporting), writing – review and editing (supporting). **Michael Brockdorff:** Investigation (supporting), writing - review and editing (supporting). **Benjamin Calmé:** Formal analysis (supporting), reviewing and editing (supporting). **Joshua Davy:** Methodology (supporting), writing - review and editing (supporting). **Vittorio Francescon:** Investigation (supporting), software (lead), writing - review and editing (supporting). **Nikita Murasovs:** Investigation (supporting), software (supporting), writing - review and editing (supporting). **Yael L. May:** Investigation (supporting), writing – review and editing (supporting). **Ryan K. Mathew:** writing – review and editing (supporting). **Russell A. Harris:** Funding acquisition (supporting), writing - review and editing (supporting). **Pietro Valdastri:** Funding acquisition (lead), supervision (supporting), writing - review and editing (supporting). **James. H Chandler:** Conceptualization (supporting), methodology (supporting), supervision (lead), validation (supporting) writing – original draft (supporting)

## Author Disclosure Statement

No competing conflicts of research or financial interest exist for this contribution.

## References


1. Runciman M, Darzi A, Mylonas GP. Soft Robotics in Minimally Invasive Surgery. Soft Robotics 2019;6(4):423-443. doi: 10.1089/soro.2018.0136.

2. Kappel AD, Jha R, Guggilapu S et al. Endovascular Applications for the Management of High-Grade Gliomas in the Modern Era. Cancers 2024;16(8):1594. doi: 10.3390/cancers16081594.

3. Srinivasan VM, Lang FF, Kan P. Intraarterial delivery of virotherapy for glioblastoma. Neurosurg Focus 2021;50(2). doi: 10.3171/2020.11.FOCUS20845.

4. Decroly G, Lambert P, Delchambre A. A Soft Pneumatic Two-Degree-of-Freedom Actuator for Endoscopy. Front Robot AI. 2021;8:768236. doi: 10.3389/frobt.2021.768236.

5. Gopesh T, Wen JH, Santiago-Dieppa D et al. Soft robotic steerable microcatheter for the endovascular treatment of cerebral disorders. Science Robotics 2021;6(57). doi: 10.1126/scirobotics.abf0601.

6. Kato T, Okumura I, Song SE et al. Tendon-Driven Continuum Robot for Endoscopic Surgery: Preclinical Development and Validation of a Tension Propagation Model. IEEE ASME Trans Mechatron. 2015;20(5):2252-2263. doi: 10.1109/TMECH.2014.2372635.

7. Kim Y, Cheng S.S. Desai J.P. Active stiffness tuning of a spring-based continuum robot for MRI-guided neurosurgery. IEEE Trans. Robot. 2018;34(1):18–28. doi: 10.1109/TRO.2017.2750692

8. Dreyfus R, Boehler Q, Lyttle S et al. Dexterous helical magnetic robot for improved endovascular access. Science Robotics 2024. doi:10.1126/scirobotics.adh0298

9. Bacchetti A, Lloyd P, Taccola S et al. Optimization and fabrication of programmable domains for soft magnetic robots: A review, Frontiers in Robotics and AI 2022;9. doi 10.3389/frobt.2022.1040984

10. da Veiga T, Chandler J.H., Lloyd P. et al. Challenges of continuum robots in clinical context: a review Progress in Biomedical Engineering 2020;2(3). doi: 10.1088/2516-1091/ab9f41.

11. Jeon S, Hoshiar AK, Kim K et al. A Magnetically Controlled Soft Microrobot Steering a Guidewire in a Three-Dimensional Phantom Vascular Network. Soft Robotics 2019;6(1):54-68. doi: 10.1089/soro.2018.0019.

12. Pittiglio G, Lloyd P, da Veiga T et al. Patient-Specific Magnetic Catheters for Atraumatic Autonomous Endoscopy. Soft Robotics 2022;9(6):1120-1133, 2022. doi: 10.1089/soro.2021.0090

13. Pittiglio G, Chandler JH, da Veiga T et al. Personalized magnetic tentacles for targeted photothermal cancer therapy in peripheral lungs. Commun Eng. 2023; 27(2):50. doi: 10.1038/s44172-023-00098-9.

14. Kim Y, Parada GA, Liu S et al. Ferromagnetic soft continuum robots. Sci Robot. 2019; 28;4(33). doi: 10.1126/scirobotics.aax7329. PMID: 33137788.

15. Hu J, Hou Y, Wangxie G et al. Magnetic Soft Catheter Robot System for Minimally Invasive Treatments of Articular Cartilage Defects. Soft Robot. 2024;11(6):1032-1042. doi: 10.1089/soro.2023.0157.

16. Lloyd P, Thomas T.L., Venkiteswaran V.K. et al. A magnetically-actuated coiling soft robot with variable stiffness IEEE Robotics and Automation Letters 2023;8(6):3262–3269. doi: 10.1109/LRA.2023.3264770.

17. Mao L, Yang P, Tian C et al. Magnetic steering continuum robot for transluminal procedures with programmable shape and functionalities, Nature Comm. 2024;15(3759). doi: 0.1038/s41467-024-48058-x

18. Kim Y, Yuk H, Zhao R et al. Printing ferromagnetic domains for untethered fast-transforming soft materials. Nature 2018; 558(7709):274-279. doi: 10.1038/s41586-018-0185-0.

19. Xue J, Zhang M, Liu X et al. A magnetic continuum robot with in-situ magnetic reprogramming capability. IEEE International Conference on Robotics and Automation (ICRA) 2-24;15(3759): 5891–5897. doi: 10.1109/ICRA57147.2024.10611450.

20. Lloyd P, Koszowska Z, Di Lecce M et al. Feasibility of fiber reinforcement within magnetically actuated soft continuum robots. Frontiers in Robotics and AI 2021; 8. doi: 10.3389/frobt.2021.715662.

21. Lloyd P, Onaizah O, Pittiglio G et al. Magnetic soft continuum robots with braided reinforcement. *IEEE Robotics and Automation Letters* 2022;7(4): 9770-9777. doi: 10.1109/LRA.2022.3191552

22. Koszowska, Z, Brockdorff, M, da Veiga, T et al. Independently Actuated Soft Magnetic Manipulators for Bimanual Operations in Confined Anatomical Cavities. Adv. Intell. Syst. 2024;6. doi: 10.1002/aisy.202300062.

23. Richter M, Kaya M, Sikorski J et al. Magnetic Soft Helical Manipulators with Local Dipole Interactions for Flexibility and Forces. Soft Robot. 2023;10(3):647-659. doi: 10.1089/soro.2022.0031.

24. Sun Y, Piskarev Y, Hofstetter EH et al. Instant variable stiffness in cardiovascular catheters based on fiber jamming. Science Advances 2025; 11(6). doi:10.1126/sciadv.adn1207

25. Wang L, Kim Y, Guo C et al. Hard-magnetic elastica. Journal of the Mechanics and Physics of Solids 2020; 142. doi: 10.1016/j.jmps.2020.104045.

26. da Veiga T, Chandler J.H., Pittiglio G et al. Material characterization for magnetic soft robots IEEE 4th International Conference on Soft Robotics (RoboSoft) 2021: 335-342. doi: 10.1109/RoboSoft51838.2021.9479189.

27. Thuillier A, Krut S Zemiti N et al. Optimal Bending Stiffness Design of a Soft Micro-Robot for Cochlear Implantation. IEEE 7th International Conference on Soft Robotics (RoboSoft) 2024: pp. 492-497. doi: 10.1109/RoboSoft60065.2024.10521998.

28. Zhang J. Simaan N. Design of Underactuated Steerable Electrode Arrays for Optimal Insertions. Journal of Mechanisms and Robotics 2013:5(1). doi: 5. 011008. 10.1115/1.4007005.

29. Abbott, J.J., Diller E, Petruska A.J. Magnetic methods in robotics. Annual Review of Control, Robotics, and Autonomous Systems 2020; 3(1):57-90vol. 3, no. 1, pp. 57–90. doi: 10.1146/annurev-control-081219-082713

30. McCutcheon J.W. Deflections and stresses in circular tapered beams and poles, Civil Engineering for Practicing and Design Engineers 1983;2: 207–233. Available from: https://www.fpl.fs.usda.gov/documnts/pdf1983/mccut83a.pdf

31. Davy J, Lloyd P, Chandler J.H. A framework for simulation of magnetic soft robots using the material point method. IEEE Robotics and Automation Letters 2023;8(6):3470–3477. doi: 10.1109/LRA.2023.3268016.

**32. Francescon V, Murasovs N, Lloyd P et al. Closed-Loop Shape-Forming Control of a Magnetic Soft Continuum Robot. IEEE Robotics and Automation Letters, 2025; 10(6). doi: 10.1109/LRA.2025.3565124**

33. Perrira N, Shuib A.S., Phang, E et al. Experimental Investigation of Blood Mimicking Fluid Viscosity for Application in 3D-Printed Medical Simulator. Journal of Physics: Conference Series 2022;2222. doi: 10.1088/1742-6596/2222/1/012016.

34. Oglat AA. A Review of Blood-mimicking Fluid Properties Using Doppler Ultrasound Applications. J Med Ultrasound. 2022;(4):251-256. doi: 10.4103/jmu.jmu_60_22.

35. Zarrinkoob L, Ambarki K, Wåhlin et al. Blood flow distribution in cerebral arteries. J Cereb Blood Flow Metab. 2015;35(4):648-54. doi: 10.1038/jcbfm.2014.241.

**36. Shoemaker L, Matern T, Kamar F et al. Blood pressure in human large cerebral arteries: a feasibility study. Journal of Applied Physiology 2025; 138:693-98. doi: https://doi.org/10.1152/japplphysiol.00825.2024**

**37. Blanco P.J., Müller L.O., Spence D. Blood pressure gradients in cerebral arteries: a clue to pathogenesis of cerebral small vessel disease. Stroke and Vascular Neurology 2017; 2(3). doi: https://doi.org/10.1136/svn-2017-000087**

38. Mount C, Das J, Cerebral perfusion pressure. StatPearls, 2023. Available from: https://www.ncbi.nlm.nih.gov/books/NBK537271/

39. Cancer imaging archive – access the data The National Institute of Health Cancer Imaging Archive 2023. Available from: https://www.cancerimagingarchive.net/access-data/

40. Davy J, Brockdorff M, Valdastri P. Utilizing Field Gradient Measurements for Object Tracking in Permanent Magnet based Manipulation Systems. IEEE Transactions on Magnetics 2025, doi: 10.1109/TMAG.2025.3553740

## Supplementary Figures

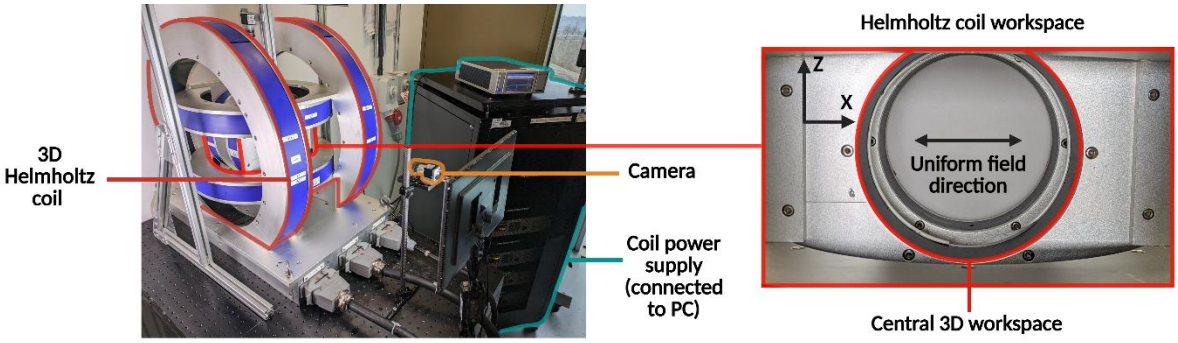


**SUPP. FIG. 1**. Annotated Helmholtz coil setup and expanded workspace view, for deflection characterization under orthogonal magnetic fields. **Created in BioRender. Bacchetti, A. (2026) https://BioRender.com/8ymarkc**

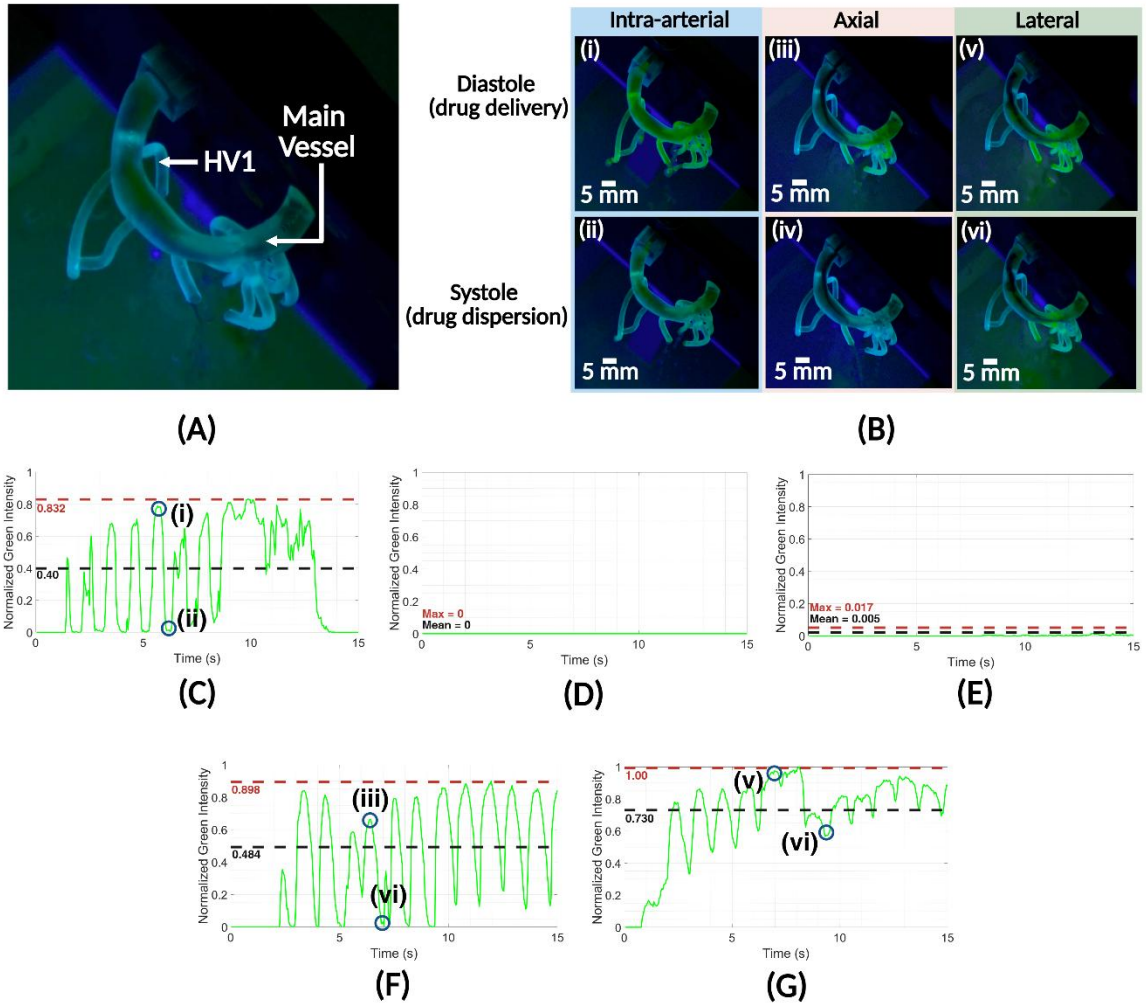


***SUPP. FIG. 2.*** *Fluorescent distribution profiles, time series and comparative profiles for intra-arterial, axial and lateral C-MSCR delivery cases throughout diastolic and systolic phases in HV2A and main vessel scenarios, (A) phantom reference with annotated vessels in correspondence with main intensity analysis points throughout delivery, (B) diastolic and systolic fluorescence profiles throughout the fifth delivery pulse. (C) intra-arterial delivery at HV2A, (D) axial C-MSCR delivery at HV2A, (E) lateral C-MSCR delivery at HV2A, (F) axial μ-channel delivery in the main vessel portion, (G) lateral μ-channel delivery in the main vessel portion.* ***Created in BioRender. Bacchetti, A. (2026) https://BioRender.com/xojk7dh***